

# AI-based separation of turbulence from coherent background flows in decaying hydrodynamic turbulence

Ji-Hoon Ha<sup>a</sup>, Elena S. Volnova<sup>b</sup>

<sup>a</sup>Korea Astronomy and Space Science Institute, 776, Daedeok-daero, Yuseong-gu, Daejeon, 34055, Republic of Korea

<sup>b</sup>Institute for Basic Science, 55, Expo-ro, Yuseong-gu, Daejeon, 34126, Republic of Korea

## Abstract

Separating turbulent fluctuations from coherent large-scale background flows is a fundamental challenge in the analysis of numerical simulations and astronomical observations. Traditional approaches to this problem commonly rely on decomposition-based techniques, including scale-based filtering methods such as Fourier or wavelet transforms, as well as adaptive methods like the Hilbert–Huang transformation. While these methods are effective and widely used, they involve subjective choices and implicitly assume that a physically meaningful separation can be achieved through scale or mode selection alone. In realistic flows, however, coherent motions and turbulent fluctuations often overlap across a broad range of scales and interact nonlinearly, rendering any clear and unique separation inherently ambiguous, particularly in astrophysical settings where data are projected or sparsely sampled. In this work, we assess the robustness of AI-based turbulence–background separation using two-dimensional incompressible Navier–Stokes simulations of decaying hydrodynamic turbulence. The simulations are initialized with a coherent background flow and divergence-free turbulent perturbations with a Kolmogorov-like power spectrum, and evolve without external forcing, providing a conservative physical testbed. A neural network trained exclusively on static synthetic images is applied to simulation snapshots at different evolutionary stages. We find that the model successfully recovers turbulent fluctuations during early and intermediate stages, when partial scale separation is preserved. At later stages, despite the substantial decay of turbulent energy and the resulting reduction in fluctuation strength, the model continues to recover visually and spectrally plausible turbulent structures and preserves inertial-range spectral scaling, demonstrating robust separation under increasingly challenging conditions. These results demonstrate the potential of applying AI models trained on static data to time-evolving turbulent flows, with direct implications for astrophysical and cosmological applications.

**Keywords:** Background separation, Deep learning, Hydrodynamic simulations, Turbulence

## 1. Introduction

Turbulent flows in natural and astrophysical environments are seldom encountered in isolation. Turbulent fluctuations are generally embedded within coherent large-scale background flows produced by global shear, stratification, rotation, or other organized motions. For instance, velocity fields in molecular clouds display pronounced large-scale gradients alongside small-scale turbulent fluctuations (e.g., Imara & Blitz, 2011; Li, 2021). Similarly, magnetic fields in molecular clouds consist of smoothly varying large-scale components superimposed with turbulence on smaller scales (e.g., Girart et al., 2006; Hildebrand et al., 2009; Houde et al., 2009; Pattle et al., 2017, 2022). Separating turbulent fluctuations from these background components has therefore remained a long-standing challenge in the analysis and interpretation of both observational data and numerical simulations.

Traditional approaches to separating turbulent fluctuations from large-scale background flows commonly rely on decomposition-based techniques, including scale-based filtering methods such as Fourier or wavelet transforms (e.g., Grebenev et al., 1995), as well as adaptive methods like the Hilbert–Huang transformation (Huang et al., 1998, 1999). In

these approaches, a cutoff scale or a selected set of modes is typically used to distinguish coherent background variations from turbulent fluctuations. While such methods are effective and widely employed, they inevitably involve subjective choices and implicitly assume that a physically meaningful separation can be achieved through scale or mode selection alone. More sophisticated multiscale statistical frameworks incorporating higher-order moments and information-theoretic measures have been developed to characterize turbulence beyond second-order statistics. However, these approaches likewise rely on multiscale decompositions and require an explicit or implicit removal of large-scale trends, rendering their interpretation sensitive to how background components are defined and subtracted (Granero-Belinchon et al., 2024). In realistic flows, coherent motions and turbulent fluctuations often coexist and overlap across a broad range of scales and interact nonlinearly, making any clear and unique separation based solely on scale inherently ambiguous (e.g., Cho, 2019). This ambiguity is further compounded in astrophysical applications, where observables are frequently projected along the line of sight and integrate contributions from multiple scales with comparable amplitudes, complicating attempts to disentangle coherent and turbulent components even when their physical scales are well mo-

tivated (Seta & Federrath, 2024). Moreover, the definition of a local, scale-dependent background field itself can influence measured statistics and intermittency, highlighting that the distinction between background and fluctuations is not uniquely defined in multiscale, anisotropic turbulent systems (Sioulas et al., 2025).

Recent advances in deep learning have opened new possibilities for turbulence–background separation by learning non-local and multi-scale features directly from data (e.g., Brunton et al., 2020). Several studies have demonstrated that neural networks can recover turbulent components with high fidelity under controlled conditions when trained on synthetic datasets constructed by linear superposition of independently generated background and turbulence fields (e.g., Ling et al., 2016; Nakamura et al., 2021). Despite these promising results, an important open question remains: whether models trained on such static and idealized data can generalize to physically realistic systems in which background flows and turbulence evolve self-consistently and interact through nonlinear dynamics (e.g., Brenner et al., 2019; Kochkov et al., 2021).

In this work, we address this question by testing an AI-based turbulence–background separation model in a time-evolving hydrodynamic setting. Specifically, we apply a neural network trained exclusively on static synthetic images to two-dimensional incompressible Navier–Stokes simulations of decaying hydrodynamic turbulence. The simulations are initialized with a coherent large-scale background flow and divergence-free turbulent perturbations with a Kolmogorov-like power spectrum, and subsequently evolve without external forcing. As the turbulent energy decays and nonlinear interactions progressively distort the background flow, the distinction between coherent and turbulent structures becomes increasingly ambiguous, providing a conservative and physically meaningful stress test for AI-based separation. Rather than proposing a new separation algorithm, the present study uses AI as a diagnostic tool to probe the physical conditions under which turbulence–background separation remains meaningful in time-evolving flows.

The goal of this study is not to construct a fully realistic model of astrophysical turbulence, but rather to assess the robustness and potential of AI-based turbulence–background separation under controlled yet physically nontrivial conditions. By systematically applying the trained model to simulation snapshots at different evolutionary stages, we aim to identify the regime in which such separation remains meaningful, as well as the conditions under which it breaks down. The paper is organized as follows. In Section 2, we describe the AI model and the construction of the synthetic training data. Section 3 presents the hydrodynamic simulations and the application of the AI model to decaying turbulent flows. Summary and discussion are provided in Section 4.

## 2. AI Model for Turbulence–Background Separation

### 2.1. Problem Definition and Training Data

We formulate turbulence–background separation as an image-to-image regression task. Given a 2D input field  $O(x, y)$

that contains a coherent large-scale background component  $B(x, y)$  and a turbulent fluctuation field  $I(x, y)$ ,

$$O(x, y) = B(x, y) + I(x, y), \quad (1)$$

the goal is to infer the turbulent component  $\hat{I}(x, y)$  from the input. For training, we construct synthetic examples where the background and turbulence are generated independently and then linearly superposed. The background component is modeled as a low-wavenumber sinusoidal pattern,

$$B(x, y) = A \sin(2\pi k_x x + \phi_1) \cos(2\pi k_y y + \phi_2), \quad (2)$$

with random phases  $(\phi_1, \phi_2)$  and randomized spatial frequencies  $(k_x, k_y)$  sampled uniformly in the range corresponding to 1–3 cycles across the  $224 \times 224$  domain. The amplitude  $A$  is randomly sampled in the range [0.3, 0.8] per sample. This construction follows the implementation in our dataset generator. Turbulent fields are generated as isotropic random-phase realizations with a Kolmogorov-like power spectrum,

$$P_I(k) \propto k^{-5/3}, \quad (3)$$

implemented by assigning Fourier amplitudes  $|\hat{I}(\mathbf{k})| \propto k^{-5/6}$  above a prescribed injection wavenumber and then transforming back to real space. The injection scale is fixed to  $\ell_{\text{inj}} = L/8$  (i.e., an injection scale ratio of 1/8), and the turbulence RMS is randomized in the range [0.05, 0.25] per sample.

The turbulence–background separation problem is formulated as an image-to-image regression task. The network input consists of a two-dimensional scalar field  $O(x, y)$  that contains both a coherent large-scale background component and small-scale turbulent fluctuations. The target output is the turbulent component  $I(x, y)$  alone. Since the data are intrinsically single-channel scalar fields, both the input and the target are represented as tensors of shape (1, 224, 224).

Fig. 1 shows representative examples of the synthetic training data. The top row displays input images constructed by linearly superposing a smooth background field and a turbulent field, while the bottom row shows the corresponding turbulence-only targets. The background component is dominated by low-wavenumber modes with coherent spatial structure, whereas the turbulent component exhibits nearly isotropic small-scale fluctuations with a Kolmogorov-like spectrum.

### 2.2. Network Architecture

Our separation model is a hybrid Transformer–CNN U-Net designed for multi-scale reconstruction. The encoder is a Swin Transformer (Swin-Tiny, patch size 4, window size 7) implemented via `timm`, and multi-scale feature maps are extracted at four resolutions corresponding to patch-embedding output and successive Swin stages (Liu et al., 2021). A schematic overview of the model architecture is shown in Fig. 2. The encoder is a Swin Transformer that operates on non-overlapping image patches and captures long-range spatial correlations through shifted self-attention windows. Multi-scale feature maps extracted at successive encoder stages are passed to the decoder through skip connections. The decoder progressively upsamples these features and reconstructs the turbulent component at

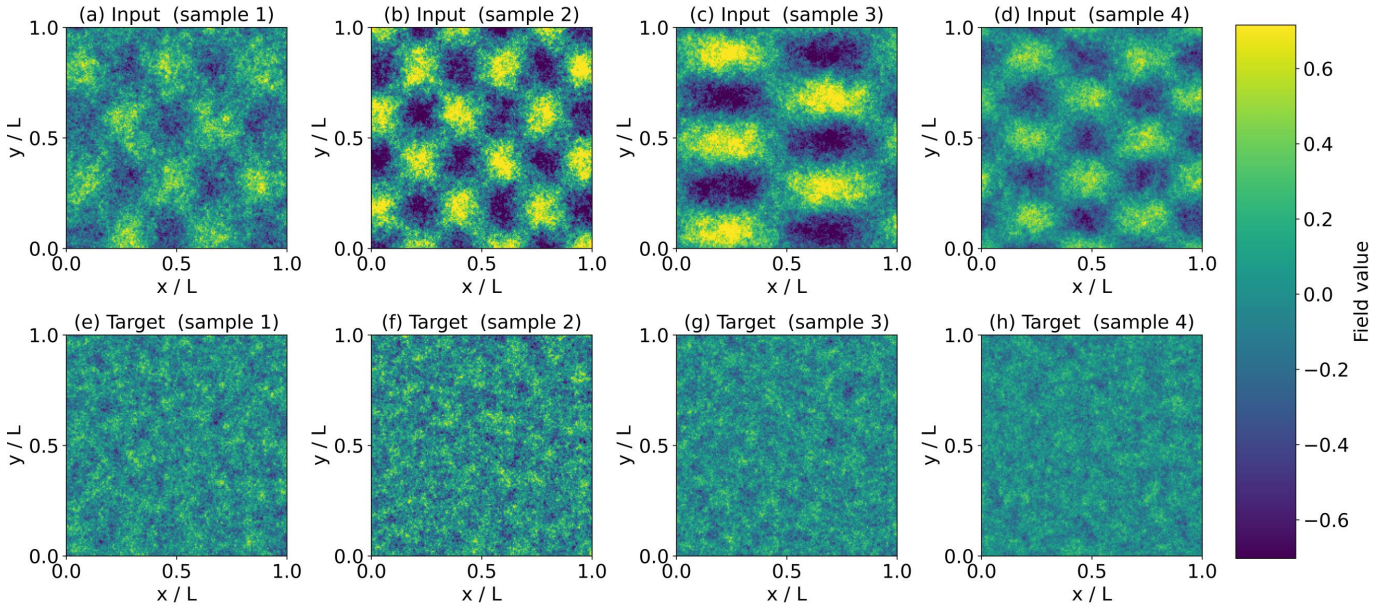


Figure 1: Representative examples of the synthetic training data used for the AI-based turbulence–background separation. The top row shows input images constructed as linear superpositions of a coherent large-scale background field and a turbulent fluctuation field ( $O(x, y) = B(x, y) + I(x, y)$ ). The bottom row shows the corresponding turbulence-only targets ( $I(x, y)$ ). The background component is dominated by low-wavenumber coherent structures, while the turbulent component exhibits small-scale, nearly isotropic fluctuations with a Kolmogorov-like power spectrum.

the original spatial resolution (Ronneberger et al., 2015). This design enables the model to distinguish between large-scale coherent patterns and small-scale turbulent structures.

Specifically, for an input image of size  $224 \times 224$ , the encoder produces feature maps at resolutions  $56^2$ ,  $28^2$ ,  $14^2$ , and  $7^2$  with nominal channel dimensions  $\{96, 192, 384, 768\}$  for Swin-Tiny. These are projected via  $1 \times 1$  convolutions to a U-Net-like set of skip features with channels  $\{64, 128, 256, 512\}$ . The decoder follows a U-Net design with bilinear upsampling, skip concatenation, and two-layer  $3 \times 3$  convolutional blocks:

- Bottleneck: a convolutional block operating at  $7 \times 7$  and 512 channels.
- Upsampling path: three upsampling blocks with skip connections ( $7 \rightarrow 14 \rightarrow 28 \rightarrow 56$ ).
- Final refinement: two additional upsampling steps without skip connections ( $56 \rightarrow 112 \rightarrow 224$ ) using convolutional blocks ( $64 \rightarrow 32$  and  $32 \rightarrow 16$ ).
- Output head: a  $1 \times 1$  convolution mapping 16 channels to the 1-channel prediction.

This architecture outputs  $\hat{I}$  at the original resolution, enabling direct comparison to the turbulence target in pixel space.

### 2.3. Loss Function

Training minimizes a composite objective designed to promote both pixel-level fidelity and physically consistent spectral content:

$$\mathcal{L} = \lambda_{\text{MSE}} \mathcal{L}_{\text{MSE}} + \lambda_{\text{spec}} \mathcal{L}_{\text{spec}} + \lambda_{\text{leak}} \mathcal{L}_{\text{leak}}. \quad (4)$$

The primary term is the mean squared error,

$$\mathcal{L}_{\text{MSE}} = \left\langle \left( \hat{I} - I \right)^2 \right\rangle, \quad (5)$$

computed over all pixels, channels, and batch elements.

To enforce spectral agreement, we add a radial power spectral density (PSD) matching term. After subtracting the spatial mean to suppress DC bias, we compute 2D FFTs using orthonormal normalization and evaluate the radially averaged PSD  $P(k)$  by binning  $|\hat{F}|^2$  on the unshifted FFT grid. We then minimize the mean squared difference of  $\log_{10} P(k)$  within a selected wavenumber band:

$$\mathcal{L}_{\text{spec}} = \left\langle [\log_{10} P_{\hat{I}}(k) - \log_{10} P_I(k)]^2 \right\rangle_{k_{\min} \leq k \leq k_{\max}}, \quad (6)$$

where we set  $k_{\min} = k_{\text{inj}}$  and  $k_{\max} = 0.35$  (in units of cycles per pixel).

Finally, to discourage contamination of the prediction by the coherent background modes, we introduce a leakage penalty based on the projection coefficient of  $\hat{I}$  onto the known background field  $B$  (available in the synthetic training set):

$$a = \frac{\langle \hat{I} B \rangle}{\langle B^2 \rangle}, \quad \mathcal{L}_{\text{leak}} = \langle a^2 \rangle, \quad (7)$$

where  $\langle \cdot \rangle$  denotes spatial averaging (and additionally averaging over batch and channels). Although the leakage term relies on knowledge of the background field and is therefore applicable only during training on synthetic data, it serves to guide the network toward a physically meaningful separation that generalizes to unseen simulation data.

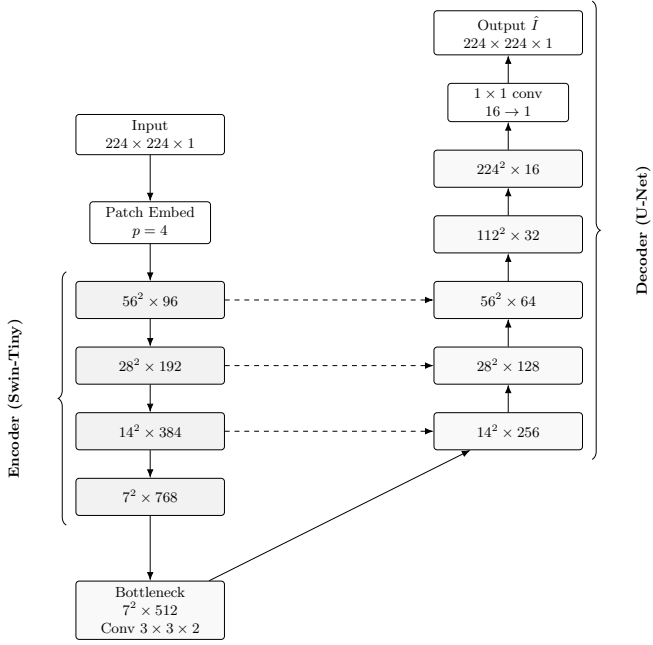


Figure 2: Architecture of the hybrid Swin Transformer–U-Net model used for turbulence–background separation. The Swin-Tiny encoder extracts hierarchical multi-scale features at resolutions  $56^2$ ,  $28^2$ ,  $14^2$ , and  $7^2$ , which are passed to a U-Net–style decoder via same-resolution skip connections. The decoder progressively upsamples the latent representation and reconstructs the target field at the original resolution. Both the input and the output are single-channel scalar fields of size  $224 \times 224$ .

In our baseline configuration, we set  $\lambda_{\text{MSE}} = 1$ ,  $\lambda_{\text{spec}} = 5 \times 10^{-3}$  and  $\lambda_{\text{leak}} = 5 \times 10^{-2}$ . The evolution of the individual loss terms during training is shown in Fig. 3. The mean squared error rapidly decreases within the first few epochs, indicating fast convergence in pixel space. The spectral loss decreases more gradually, reflecting the increased difficulty of matching the power spectrum across spatial scales. The leakage loss remains subdominant but non-negligible, demonstrating that the model actively suppresses contamination from large-scale background modes.

#### 2.4. Model Training and Results

We train the model using AdamW optimizer (Loshchilov & Hutter, 2019) with a learning rate of  $10^{-3}$  for 40 epochs, with batch size 32 on a dataset of 1024 synthetic images. In addition, we reserve 128 images for validation during training to monitor convergence and prevent overfitting, and a separate set of 128 images is used for testing and quantitative evaluation. The trained weights are stored for later inference on hydrodynamic simulation snapshots, which represent a more challenging regime because the background and turbulence evolve self-consistently and interact nonlinearly over time.

Fig. 4 presents representative examples of the model performance on independent test samples. For each case, the true turbulent field, the model prediction, and the residual are shown. The predicted turbulence closely reproduces the spatial morphology of the true field, while the residuals are largely featureless and dominated by low-amplitude noise. This demonstrates

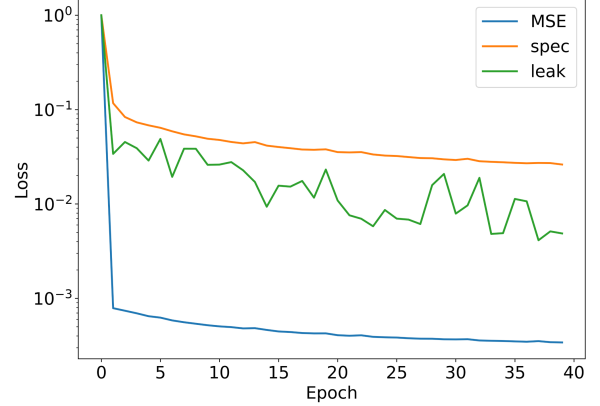


Figure 3: Evolution of the loss components during training. The total loss (solid black line) is composed of a pixel-wise mean squared error term, a spectral consistency term, and a leakage penalty that suppresses contamination from background modes. The rapid decrease of the MSE indicates fast convergence in pixel space, while the more gradual decay of the spectral loss reflects the increasing difficulty of matching power spectra across spatial scales.

that the model successfully isolates turbulent fluctuations without imprinting coherent background structures.

To quantify the spectral accuracy of the separation, we compute power spectra for 128 independent test samples and average them. Fig. 5 compares the mean power spectrum of the true turbulence with that of the model prediction. The predicted spectrum closely follows the true spectrum over a broad range of wavenumbers, including the inertial range, with deviations appearing only at the highest wavenumbers where numerical dissipation and finite resolution effects dominate.

### 3. Application to Decaying Hydrodynamic Turbulence

The AI model is trained exclusively on static synthetic data in which the background and turbulence components are linearly superposed and do not interact. In contrast, physically realistic flows are governed by nonlinear dynamics, in which coherent structures and turbulence evolve self-consistently. To assess the robustness and generalization capability of the model, we apply it to two-dimensional incompressible Navier–Stokes simulations of decaying hydrodynamic turbulence.

In this section, we primarily describe the numerical setup used to simulate decaying hydrodynamic turbulence in two dimensions. The simulations are designed to provide a controlled physical testbed in which an initially imposed large-scale coherent flow interacts nonlinearly with freely decaying turbulence, a setting that has been widely used to study the emergence of coherent structures and late-time organization in two-dimensional incompressible flows (e.g., Kraichnan & Montgomery, 1980; Matthaeus et al., 1991; Dmitruk et al., 1996). No external forcing is applied after the initial time, allowing us to isolate the intrinsic evolution of turbulence and its interaction with the background flow. This setup is particularly suited for assessing the robustness of AI-based turbulence–background separation models under time-evolving flow conditions. We then apply a neural network trained on static synthetic data to snapshots of

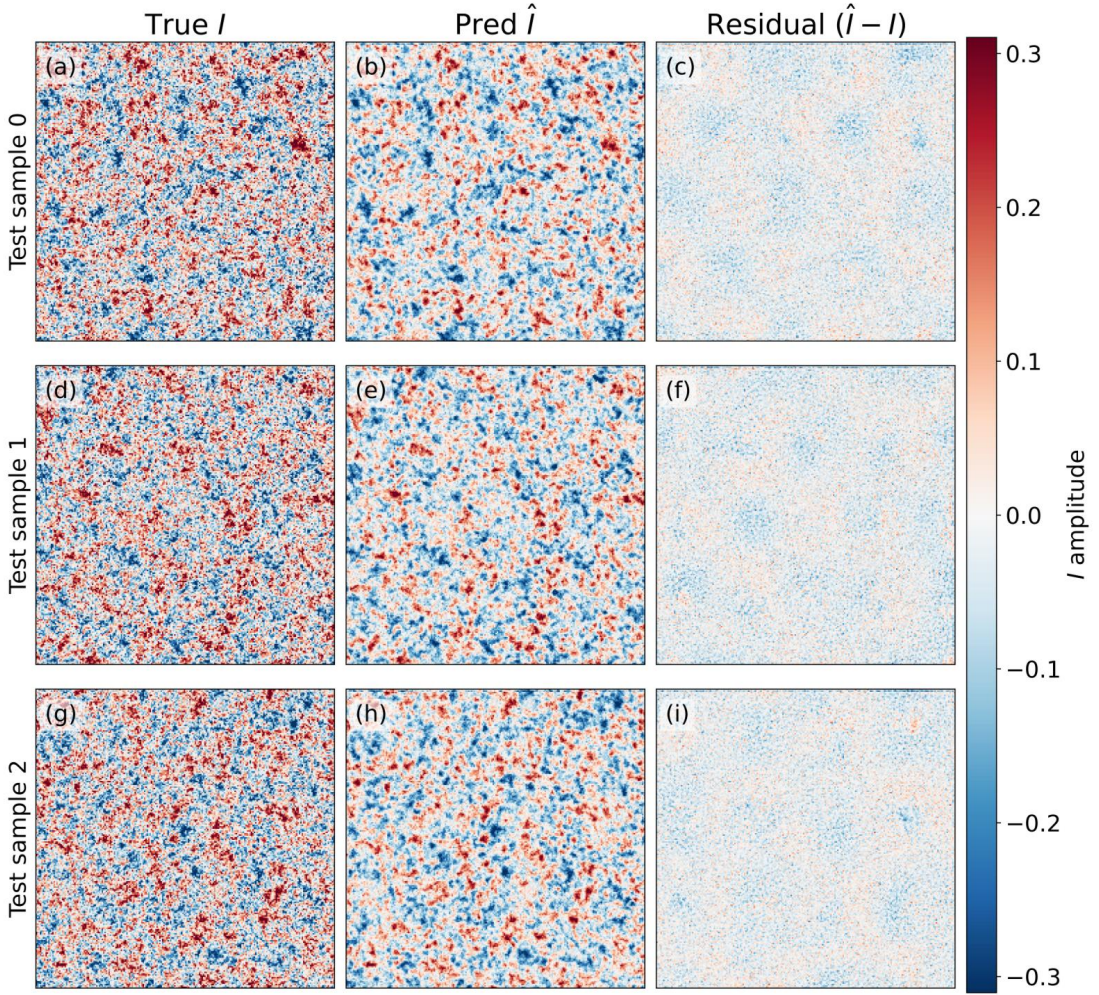


Figure 4: Example results of the turbulence–background separation on independent synthetic test samples. From left to right, each column shows the true turbulent field, the model prediction, and the residual. The predicted turbulence closely reproduces the spatial morphology of the true field, while the residuals are largely featureless and dominated by low-amplitude noise, indicating successful suppression of background structures.

the evolving simulations and analyze its ability to recover turbulent fluctuations through a combination of spectral and energy-based diagnostics.

### 3.1. Governing Equations

We simulate two-dimensional incompressible turbulence by solving the Navier–Stokes equations in vorticity–streamfunction form. Under the incompressibility condition,

$$\nabla \cdot \mathbf{u} = 0, \quad (8)$$

the evolution of the vorticity  $\omega$  is governed by

$$\frac{\partial \omega}{\partial t} + \mathbf{u} \cdot \nabla \omega = \nu \nabla^2 \omega + f, \quad (9)$$

where  $\nu$  is the kinematic viscosity and  $f$  represents an external forcing term. In the decaying turbulence experiments discussed in this work, we set  $f = 0$ .

In two dimensions, the velocity field  $\mathbf{u} = (u, v)$  is expressed in terms of the streamfunction  $\psi$  as

$$u = \frac{\partial \psi}{\partial y}, \quad v = -\frac{\partial \psi}{\partial x}, \quad (10)$$

and the vorticity is given by

$$\omega = \nabla^2 \psi. \quad (11)$$

At each time step, the Poisson equation for  $\psi$  is solved in Fourier space to recover the velocity field from the vorticity field.

### 3.2. Computational Domain and Non-dimensionalization

The simulations are performed in a doubly periodic square domain,

$$(x, y) \in [0, L_x) \times [0, L_y), \quad (12)$$

with  $L_x = L_y = 1$ . All quantities are expressed in non-dimensional units. Consequently, the simulation time  $t$  should

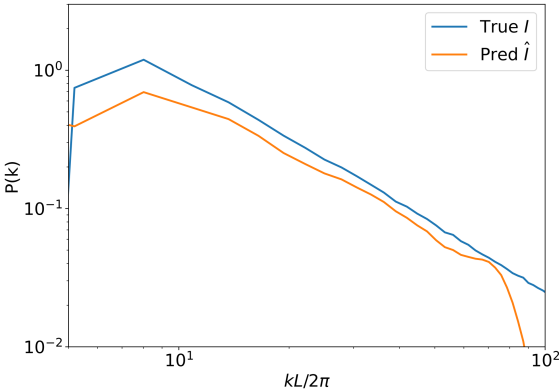


Figure 5: Comparison of the radially averaged power spectra for the true turbulence and the AI-predicted turbulence, averaged over 128 independent test samples. The predicted spectrum closely follows the true spectrum over a broad range of wavenumbers, including the inertial range, with deviations appearing only at the highest wavenumbers where finite-resolution and numerical dissipation effects become significant.

be interpreted as a dimensionless time measured in units of the characteristic flow crossing time,  $\tau \sim L/U$ , where  $U$  is a representative velocity scale of the system.

### 3.3. Pseudo-spectral Method and De-aliasing

Spatial derivatives are computed using a pseudo-spectral method based on Fourier transforms. In Fourier space, derivatives are evaluated exactly via

$$\partial_x \rightarrow ik_x, \quad \partial_y \rightarrow ik_y, \quad \nabla^2 \rightarrow -k^2, \quad (13)$$

where  $k^2 = k_x^2 + k_y^2$ .

The streamfunction in Fourier space is obtained from the vorticity spectrum as

$$\hat{\psi}(\mathbf{k}) = -\frac{\hat{\omega}(\mathbf{k})}{k^2}, \quad (k \neq 0), \quad (14)$$

with the zero mode set to zero. The velocity components are then reconstructed via

$$\hat{u} = ik_y \hat{\psi}, \quad \hat{v} = -ik_x \hat{\psi}. \quad (15)$$

The nonlinear advection term  $\mathbf{u} \cdot \nabla \omega$  is evaluated in real space following the standard pseudo-spectral procedure. To suppress aliasing errors arising from nonlinear mode coupling, the 2/3 de-aliasing rule is applied by truncating Fourier modes whose wavenumbers exceed two-thirds of the maximum resolvable wavenumber.

### 3.4. Time Integration

Time integration is performed using a second-order Runge–Kutta (RK2) scheme. Given the right-hand side operator  $R(\omega)$ , the update from time level  $n$  to  $n + 1$  reads

$$\omega^{(1)} = \omega^n + \Delta t R(\omega^n), \quad (16)$$

$$\omega^{n+1} = \omega^n + \frac{\Delta t}{2} [R(\omega^n) + R(\omega^{(1)})]. \quad (17)$$

De-aliasing is applied after each sub-step.

## 3.5. Initial Conditions

### 3.5.1. Coherent Background Flow

The large-scale background flow is constructed using a streamfunction of the form

$$\psi_{\text{bg}}(x, y) = A_\psi \sin(2\pi k_x x + \phi_1) \cos(2\pi k_y y + \phi_2), \quad (18)$$

where  $k_x$  and  $k_y$  denote the number of cycles across the domain, and  $\phi_1, \phi_2$  are random phases.

A key implementation detail is that the parameter controlling the background amplitude is defined in terms of the target velocity root-mean-square (RMS),

$$u_{\text{rms,bg}} = \left[ \frac{1}{2} (\langle u^2 \rangle + \langle v^2 \rangle) \right]^{1/2}, \quad (19)$$

rather than the streamfunction amplitude  $A_\psi$ . After constructing the background streamfunction, the entire field is rescaled so that the resulting velocity field attains the prescribed RMS value. This normalization ensures numerical stability and provides a physically intuitive control parameter.

### 3.5.2. Turbulent Perturbations

Divergence-free turbulent perturbations are added to the background flow at the initial time. The turbulent component is generated in Fourier space using a random-phase streamfunction spectrum designed to approximate a target energy spectrum,

$$E(k) \propto k^s, \quad (20)$$

with  $s = -5/3$  in this study. The perturbations are confined to a finite injection band centered around a characteristic wavenumber  $k_{\text{inj}}$ .

The initial turbulent velocity amplitude is specified relative to the background RMS via

$$u_{\text{rms,turb}}(t = 0) = \text{turb\_ratio} \times u_{\text{rms,bg}}. \quad (21)$$

The total initial vorticity field is therefore

$$\omega(t = 0) = \omega_{\text{bg}}(t = 0) + \omega_{\text{turb}}(t = 0). \quad (22)$$

## 3.6. Simulation Parameters and Stability Monitoring

The simulations presented in this work adopt the following parameters:

- Grid resolution:  $N_x = N_y = 224$
- Domain size:  $L_x = L_y = 1$
- Kinematic viscosity:  $\nu = 2 \times 10^{-3}$
- Time step:  $\Delta t = 10^{-4}$
- Total number of steps: 10000
- Output cadence: every 500 steps
- Background RMS velocity:  $u_{\text{rms,bg}} = 1.0$
- Turbulence-to-background ratio:  $\text{turb\_ratio} = 0.2$

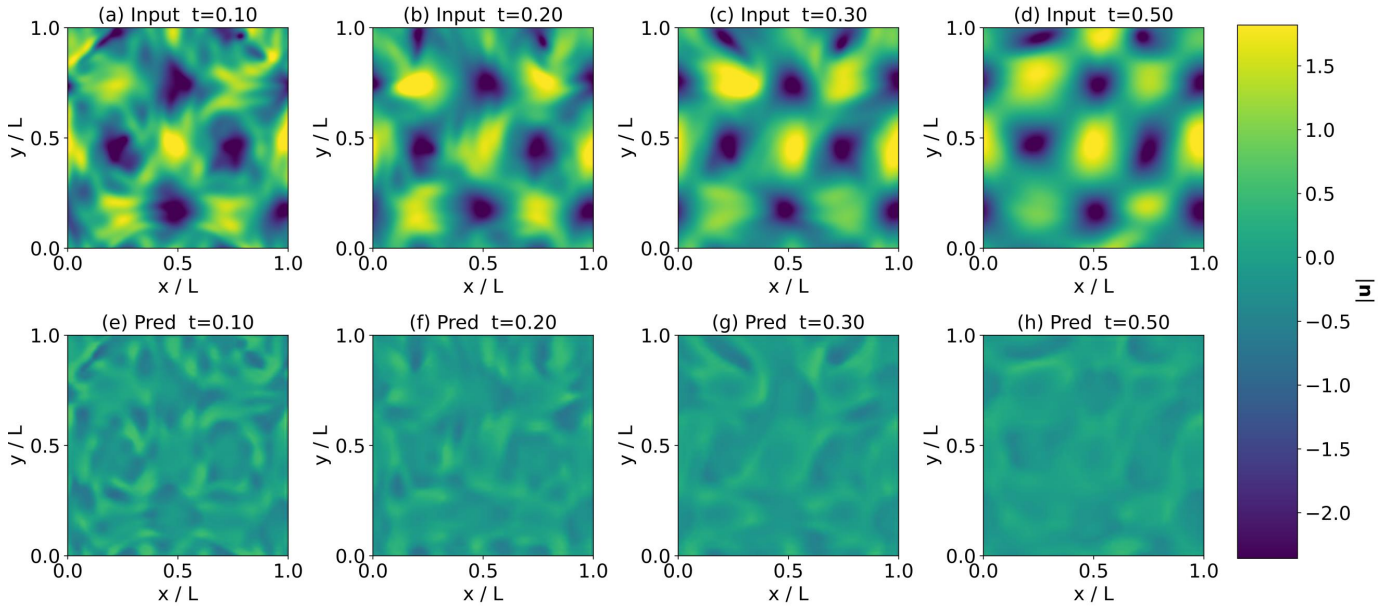


Figure 6: Application of the trained AI model to snapshots from a two-dimensional incompressible Navier–Stokes simulation of decaying hydrodynamic turbulence. The top row shows the original simulation fields containing both coherent large-scale background flow and turbulent fluctuations. The bottom row shows the turbulence fields extracted by the AI model. At early times, the background flow is effectively removed, while at later times the model continues to recover visually plausible turbulent structures despite increasing nonlinear distortion of the background.

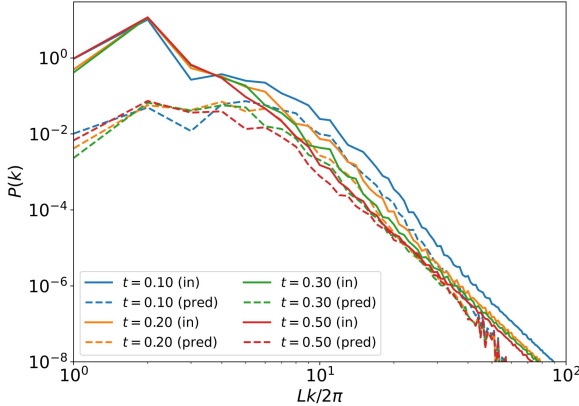


Figure 7: Power spectra of the original simulation fields and the AI-extracted turbulence at multiple simulation times. The removal of large-scale power at low wavenumbers is clearly visible in the AI-processed fields, while the inertial-range scaling at higher wavenumbers is largely preserved. This demonstrates that the AI model performs an effective scale-selective separation consistent with the physical notion of turbulence, even in a time-evolving nonlinear system. No retraining or fine-tuning was performed on the model when applied to the simulation data shown here.

- Injection scale:  $Lk_{\text{inj}}/2\pi = 8$

No external forcing is applied in the decaying turbulence runs. Each snapshot stores the velocity field  $(u, v)$ , the vorticity  $\omega$ , and the isotropically averaged energy spectrum, enabling detailed analyses of spectral evolution, background–turbulence interaction, and AI-based separation performance.

Numerical stability is monitored through a CFL-like condi-

tion,

$$\text{CFL} \approx \frac{u_{\max} \Delta t}{\Delta x}, \quad (23)$$

where  $u_{\max}$  is the maximum velocity magnitude at a given time and  $\Delta x = L_x/N_x$ . In all simulations, the CFL number remains well below unity, ensuring stable time integration.

### 3.7. Results

The present simulation is not intended as a fully realistic model of astrophysical turbulence, which is typically continuously forced. Instead, it provides a controlled physical testbed in which a coherent large-scale background flow interacts nonlinearly with decaying turbulence. This setup is particularly well suited for assessing the robustness and generalization of AI-based methods trained on static snapshots when applied to time-evolving, physically interacting flow fields. Although the simulation is two-dimensional, the controlled nature of the setup allows us to isolate the effects of nonlinear scale interaction on the separation task.

In the absence of external forcing, the turbulent energy decays monotonically with time, and the distinction between turbulent fluctuations and coherent large-scale structures becomes progressively less well defined. At sufficiently late times, the turbulent component is energetically subdominant and strongly entangled with the evolving background flow, rendering any turbulence–background separation intrinsically ambiguous. For this reason, we focus our analysis on the interval  $t \leq 0.5$ , during which the turbulent band remains dynamically significant and the separation problem is physically meaningful. Beyond this

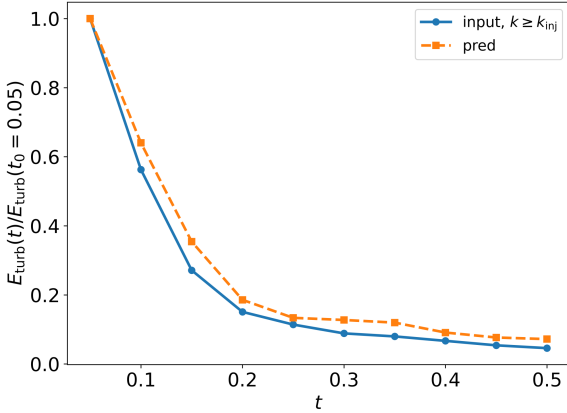


Figure 8: Time evolution of the turbulent-band energy inferred from the input (solid line) and AI-recovered (dashed line) fields. The turbulent energy is defined as  $E_{\text{turb}}(t) = \sum_{k \geq k_{\text{inj}}} P(k, t)$ , where  $k_{\text{inj}}$  corresponds to  $Lk_{\text{inj}}/2\pi = 8$ , and is normalized by its value at the earliest available time ( $t_0 = 0.05$ ). Although the input field contains both coherent and turbulent components, restricting the spectral integration to  $k \geq k_{\text{inj}}$  ensures that the measured energy predominantly traces the turbulent contribution. The close agreement between the two curves demonstrates that the AI model robustly captures the temporal decay of the turbulent energy despite increasing spectral overlap at later times.

stage, further degradation of the separation reflects the intrinsic ambiguity of the problem rather than a change in the behavior or robustness of the AI model.

Fig. 6 shows snapshots of the hydrodynamic simulation at several times, together with the corresponding outputs of the AI model. The top row displays the original simulation fields containing both large-scale background flow and turbulent fluctuations. The bottom row shows the turbulence fields extracted by the AI model. At early times, the predicted turbulence closely resembles the small-scale structures present in the original flow, while the coherent background patterns are effectively removed. As time progresses, the background flow becomes increasingly distorted by nonlinear interactions, yet the model continues to extract a visually plausible turbulent component.

The scale-dependent performance of the turbulence–background separation is quantified in Fig. 7, which compares the power spectra of the original simulation fields and the AI-extracted turbulence at multiple times. In all cases, the removal of large-scale power at low wavenumbers is clearly visible, while the inertial-range scaling at higher wavenumbers is largely preserved. This demonstrates that the AI model performs an effective large-scale filtering that is consistent with the physical notion of turbulence, even in a time-evolving nonlinear system.

As a complementary and physically transparent diagnostic, we examine the time evolution of the turbulent-band energy inferred from the input and AI-recovered fields. The turbulent energy is defined as

$$E_{\text{turb}}(t) = \sum_{k \geq k_{\text{inj}}} P(k, t) 2\pi k \Delta k, \quad (24)$$

with  $Lk_{\text{inj}}/2\pi = 8$ , and is normalized by its value at the earliest available time. Although the input field contains both coherent

and turbulent components, restricting the spectral integration to  $k \geq k_{\text{inj}}$  ensures that the measured energy predominantly traces the turbulent contribution. As shown in Fig. 8, the turbulent energy extracted from the AI-recovered field exhibits a decay trend that closely follows that of the input field over the entire interval  $t \leq 0.5$ . Both curves show a rapid early-time decay followed by a more gradual decline at later times, indicating that the model captures the overall temporal evolution of the turbulent energy despite increasing spectral overlap between coherent and turbulent structures. The systematic offset between the two curves, with the recovered energy remaining slightly higher at late times, is consistent with residual contamination from large-scale components and does not indicate a qualitative mismatch in the decay behavior. These results demonstrate that, while the separation becomes increasingly ambiguous at later stages, the AI model robustly tracks the global energy decay of the turbulent band in a physically meaningful manner.

#### 4. Summary and Discussion

In this work, we have investigated the robustness of an AI-based turbulence–background separation model when applied to physically time-evolving hydrodynamic flows. The model was trained exclusively on static synthetic data constructed as linear superpositions of a coherent background component and a turbulent fluctuation field. Despite this highly idealized training setup, we demonstrated that the model can successfully extract turbulent structures from snapshots of two-dimensional incompressible Navier–Stokes simulations in which the background flow and turbulence evolve self-consistently and interact nonlinearly. This result indicates that the AI model is capable of generalizing beyond the specific statistical properties of the training data, provided that a meaningful physical distinction between coherent and turbulent scales is retained.

A key aspect of this study is the use of decaying hydrodynamic turbulence as a testbed. Unlike forced turbulence, decaying turbulence represents a conservative scenario in which no additional energy is injected and the separation between large-scale and small-scale structures becomes progressively more challenging over time. As the turbulent energy decays and nonlinear interactions distort the initially coherent background flow, the amplitude of turbulent fluctuations decreases and the distinction between background and turbulence becomes increasingly subtle. Nevertheless, the AI model continues to recover visually and spectrally plausible small-scale turbulent structures, even when the turbulent energy has significantly decayed, providing a stringent test of its robustness under adverse conditions.

Our results also provide insight into what the AI model has learned. The successful recovery of turbulent fluctuations is not equivalent to a simple high-pass filtering or smoothing operation. Instead, the preservation of inertial-range spectral scaling, together with the suppression of low-wavenumber power associated with the background flow, suggests that the model has learned a scale-selective representation of turbulence that is consistent with its physical definition. This interpretation is

further supported by the fact that the model maintains reasonable performance even when the background flow is substantially deformed relative to the training examples, indicating that the separation relies on more than purely morphological pattern matching.

The temporal evolution of the simulation data allows us to identify a natural failure boundary for the AI-based separation. At sufficiently late times (i.e.,  $t > 0.5$ ), when nonlinear interactions lead to strong spectral overlap between background and turbulent components, we interpret the degradation of the AI output as reflecting an intrinsic physical ambiguity rather than a deficiency of the model architecture or training procedure. Explicitly identifying this temporal boundary is an important outcome of the present study, as it clarifies the conditions under which AI-based turbulence–background separation can be meaningfully applied.

Although the present work is limited to two-dimensional incompressible flows and decaying turbulence, the approach provides a clear framework for future extensions. Natural next steps include the application to forced turbulence, fully three-dimensional flows, and compressible systems more directly relevant to astrophysical environments. In addition, incorporating temporal information explicitly into the AI architecture may further improve robustness in strongly time-dependent regimes. Overall, this study demonstrates that decaying hydrodynamic turbulence offers a physically meaningful and conservative benchmark for evaluating AI-based turbulence–background separation, and highlights both the potential and the limitations of applying deep-learning models trained on static data to dynamically evolving turbulent systems. We therefore emphasize that AI-based separation should not be interpreted as defining a unique physical decomposition, but rather as providing a data-driven diagnostic whose validity depends on the underlying flow regime.

## Acknowledgements

The authors thank the referees for their comments and suggestions, which have improved the quality of this manuscript.

## References

M. P. Brenner, J. D. Eldredge, and J. B. Freund, “Perspective on machine learning for advancing fluid mechanics,” *Phys. Rev. Fluids* **4**(10), 100501 (2019).

S. L. Brunton, B. R. Noack, and P. Koumoutsakos, “Machine Learning for Fluid Mechanics,” *Annu. Rev. Fluid Mech.* **52**, 477–508 (2020).

J. Cho, “A Technique for Removing Large-scale Variations in Regularly and Irregularly Spaced Data,” *Astrophys. J.* **874**(1), 75 (2019).

P. Dmitruk, D. Gómez, A. Costa, and S. Ponce Dawson, “Asymptotic states of decaying turbulence in two-dimensional incompressible flows,” *Phys. Rev. E* **54**(3), 2555–2563 (1996).

J. M. Girart, R. Rao, and D. P. Marrone, “Magnetic Fields in the Formation of Sun-Like Stars,” *Science* **313**(5788), 812–814 (2006).

C. Granero-Belinchon, S. G. Roux, and N. B. Garnier, “Multiscale and anisotropic characterization of images based on complexity: An application to turbulence,” *Physica D* **459**, 134027 (2024).

S. A. Grebenev, W. Forman, C. Jones, and S. Murray, “Wavelet Transform Analysis of the Small-Scale X-Ray Structure of the Cluster Abell 1367,” *Astrophys. J.* **445**, 607 (1995).

R. H. Hildebrand, L. Kirby, J. L. Dotson, M. Houde, and J. E. Vaillancourt, “Dispersion of Magnetic Fields in Molecular Clouds. I,” *Astrophys. J.* **696**(1), 567 (2009).

M. Houde, J. E. Vaillancourt, R. H. Hildebrand, S. Chitsazadeh, and L. Kirby, “Dispersion of Magnetic Fields in Molecular Clouds. II,” *Astrophys. J.* **706**(2), 1504 (2009).

N. E. Huang, Z. Shen, S. R. Long, M. C. Wu, H. H. Shih, Q. Zheng, N.-C. Yen, C. C. Tung, and H. H. Liu, “The empirical mode decomposition and the Hilbert spectrum for nonlinear and non-stationary time series analysis,” *Proc. R. Soc. A* **454**(1971), 903–995 (1998).

N. E. Huang, Z. Shen, and S. R. Long, “A New View of Nonlinear Water Waves: The Hilbert Spectrum,” *Annu. Rev. Fluid Mech.* **31**, 417–457 (1999).

N. Imara and L. Blitz, “Angular Momentum in Giant Molecular Clouds. I. The Milky Way,” *Astrophys. J.* **732**(2), 78 (2011).

D. Kochkov, J. A. Smith, A. Alieva, Q. Wang, M. P. Brenner, and S. Hoyer, “Machine learning–accelerated computational fluid dynamics,” *Proc. Natl. Acad. Sci. USA* **118**(21), e2101784118 (2021).

R. H. Kraichnan and D. Montgomery, “Two-dimensional turbulence,” *Rep. Prog. Phys.* **43**(5), 547 (1980).

H.-B. Li, “Magnetic Fields in Molecular Clouds—Observation and Interpretation,” *Galaxies* **9**(2), 41 (2021).

J. Ling, A. Kurzawski, and J. Templeton, “Reynolds averaged turbulence modelling using deep neural networks with embedded invariance,” *J. Fluid Mech.* **807**, 155–166 (2016).

Z. Liu, Y. Lin, Y. Cao, H. Hu, Y. Wei, Z. Zhang, S. Lin, and B. Guo, “Swin Transformer: Hierarchical Vision Transformer using Shifted Windows,” arXiv:2103.14030 (2021).

I. Loshchilov and F. Hutter, “Decoupled Weight Decay Regularization,” arXiv:1711.05101 (2019).

W. H. Matthaeus, W. T. Stribling, D. Martinez, S. Oughton, and D. Montgomery, “Decaying, two-dimensional, Navier–Stokes turbulence at very long times,” *Physica D* **51**(1), 531–538 (1991).

T. Nakamura, K. Fukami, K. Hasegawa, Y. Nabae, and K. Fukagata, “Convolutional neural network and long short-term memory based reduced order surrogate for minimal turbulent channel flow,” *Phys. Fluids* **33**(2), 025116 (2021).

K. Pattle, D. Ward-Thompson, D. Berry, J. Hatchell, H.-R. Chen, A. Pon, P. M. Koch, W. Kwon, J. Kim, P. Bastien, J. Cho, S. Coudé, J. Di Francesco, G. Fuller, R. S. Furuya, S. F. Graves, D. Johnstone, J. Kirk, J. Kwon, C. W. Lee, B. C. Matthews, J. C. Mottram, H. Parsons, S. Sadavoy, H. Shinnaga, A. Soam, T. Hasegawa, S.-P. Lai, K. Qiu, and P. Friberg, “The JCMT BISTRO Survey: The Magnetic Field Strength in the Orion A Filament,” *Astrophys. J.* **846**(2), 122 (2017).

K. Pattle, L. Fissel, M. Tahani, T. Liu, and E. Ntormousi, “Magnetic fields in star formation: from clouds to cores,” arXiv:2203.11179 (2022).

O. Ronneberger, P. Fischer, and T. Brox, “U-Net: Convolutional Networks for Biomedical Image Segmentation,” in *Medical Image Computing and Computer-Assisted Intervention – MICCAI 2015*, pp. 234–241 (2015).

A. Seta and C. Federrath, “Structure functions with higher-order stencils as a probe to separate small- and large-scale magnetic fields,” *Mon. Not. R. Astron. Soc.* **533**(2), 1875–1886 (2024).

N. Sioulas, T. Zikopoulos, C. Shi, M. Velli, T. A. Bowen, A. Mallet, B. D. G. Chandran, L. Sorriso-Valvo, M. M. Martinović, S. S. Cerri, A. Verdini, N. Davis, and C. Dunn, “Higher-order Analysis of Three-dimensional Anisotropy in Imbalanced Alfvénic Turbulence,” *Astrophys. J.* **993**(1), 142 (2025).